THE ASTROPHYSICAL JOURNAL, 488:317–329, 1997 October 10

ROTATION IN THE PROTOSTELLAR ENVELOPES AROUND IRAS 04169+2702 AND IRAS 04365+2535: THE SIZE SCALE FOR DYNAMICAL COLLAPSE

NAGAYOSHI OHASHI,[1,2] MASAHIKO HAYASHI,[3] PAUL. T. P. HO,[1] MUNETAKE MOMOSE,[4] MOTOHIDE TAMURA,[3] NAOMI HIRANO,[5] AND ANNEILA I. SARGENT[6]

Received 1997 January 27; accepted 1997 May 13

ABSTRACT

We report interferometric observations of two embedded protostar candidates, IRAS 04169+2702 and IRAS 04365+2535 (TMC-1A), in the Taurus molecular cloud. The $C^{18}O$ $J = 1$–0 emission from IRAS 04169+2702 reveals a flattened envelope 2200 AU × 1100 AU in size; there is a velocity gradient along the elongation axis, which in turn is perpendicular to the outflow direction. Since the rotational velocity corrected for inclination, 0.23 km s^{-1} at 370 AU, gives an unacceptably small dynamical mass of 0.02 $M_\odot$ within that radius, we speculate that there is additional radial motion, possibly infall, in the flattened envelope. Around IRAS 04365+2535, a compact ^{13}CO $J = 1$–0 condensation ~1400 AU in size was detected. Again, the velocity gradient is perpendicular to the associated molecular outflow, but a rotation velocity of 0.87 km s^{-1} at 580 AU radius is consistent with the condensation being a rotationally supported disk.

Combining our new data for the two sources with published observations of rotationally supported disks and infalling envelopes around five young stars associated with the Taurus molecular cloud enables us to compare local specific angular momenta of a significant sample of these sources on scales of 200–2000 AU with those of dense cores on 6000–80,000 AU (0.03–0.4 pc) scales. The specific angular momenta for infalling envelopes and rotationally supported disks are relatively constant, ~10^{-3} km s^{-1} pc, and are typically an order of magnitude smaller than those for dense cores. These results can be explained if the dynamical collapse of dense star-forming cores takes place inside radii of ~0.03 pc while the region outside this radius remains dynamically stable.

Subject headings: circumstellar matter — ISM: kinematics and dynamics — radio lines: stars — stars: formation — stars: individual (IRAS 04169+2702, IRAS 04365+2535) — stars: pre–main-sequence

1. INTRODUCTION

Recent high-sensitivity interferometric observations of low-mass embedded sources have revealed the detailed kinematics of the surrounding flattened envelopes with typical size scales of ~1000 AU. In the Taurus molecular cloud, one of the nearest low-mass star-forming regions, high-resolution observations show infalling motions in the circumstellar envelopes around three embedded sources, HL Tau, L1551 IRS 5, and IRAS 04368+2557 (Hayashi, Ohashi, & Miyama 1993; Ohashi et al. 1996a; Saito et al. 1996; Ohashi et al. 1997). The detected motions are consistent with dynamical infall around a central star of a few tenths of a solar mass. In addition to the infalling motion, rotation has also been identified in these protostellar envelopes, with the rotational velocity 3–5 times smaller than the infall velocity at a radius of ~1000 AU. These observations demonstrate that the envelopes are not rotationally supported on scales of ~1000 AU. Since the rotational velocity scales as R^{-1} to conserve angular momentum (where R is the distance from the central protostar), whereas the infall velocity varies as $R^{-1/2}$, the rotational velocity will surpass the infall velocity only at radii more than an order of magnitude smaller than the envelope size. This provides a natural explanation for the existence of rotationally supported, possibly Keplerian disks ~100 AU in size inside the infalling envelopes (Lin et al. 1994), which are commonly observed around T Tauri stars (e.g., Beckwith et al. 1990).

The number of 1000 AU–scale protostellar envelopes studied in detail is, however, still too small for us to derive a general picture of the formation of 100 AU–scale disks or of the kinematics of protostellar envelopes. We have therefore made new interferometric observations of the two embedded sources IRAS 04169+2702 (hereafter I04169) and IRAS 04365+2535 (hereafter I04365), both associated with the Taurus molecular cloud, in order to study more examples of the kinematics of envelopes around embedded sources. I04169, with $L_{bol} \sim 0.76\ L_\odot$ (Kenyon, Calvet, & Hartmann 1993), is associated with the B217 molecular cloud, while I04365, $L_{bol} \sim 2.4\ L_\odot$ (Myers et al. 1987), is located at the center of the L1534 (TMC-1A) dense core (Benson & Myers 1989). Both sources have ^{12}CO outflows (Moriarty-Schieven et al. 1992; Bontemps et al. 1996) whose detailed outflow structures have been investigated through interferometric observations (Tamura et al. 1997, 1996; Chandler et al. 1996). Although compact circumstellar envelopes around the two sources have been mapped in CS $J = 2$–1 (Ohashi et al. 1991, 1996b), poor velocity and angular resolution precluded any detailed kinematic study.

Our new observations show that both sources are associated with rotating circumstellar envelopes. We will discuss

[1] Harvard-Smithsonian Center for Astrophysics, 60 Garden Street, Cambridge, MA 02138.
[2] nohashi@cfa.harvard.edu.
[3] National Astronomical Observatory, Mitaka, Tokyo 181, Japan.
[4] Department of Astronomical Science, Graduate University for Advanced Studies, Nobeyama, Minamimaki, Minamisaku, Nagano 384-13, Japan.
[5] Hitotsubashi University, Naka 2-1, Kunitachi, Tokyo 186, Japan.
[6] Division of Physics, Mathematics, and Astronomy, California Institute of Technology 105-24, Pasadena, CA 91125.

TABLE 1

OBSERVATION PARAMETERS

Parameter	IRAS 04169+2702	IRAS 04365+2535
Array	Owens Valley Millimeter Array	Nobeyama Millimeter Array
Number of elements	10.4 m × 6	10 m × 6[a]
Observation date	1995 February and April	1993 December and 1995 February
Number of configurations	3 (H, E, and L)	2 (C and D)
Observed species	^{13}CO $J = 1$–0, C^{18}O $J = 1$–0, and 2.7 mm continuum	^{13}CO $J = 1$–0 and 2.7 mm continuum
Front end	Cooled SIS	Cooled SIS
Back end	Digital (for line) and analog (for continuum) correlators	Digital correlator (FX)
System noise temperature[b]	250–500 K (SSB)	300–400 K (DSB)
Velocity resolution (for line)	0.34 km s^{-1}	0.43 km s^{-1}
Total bandwidth (for continuum)	1 GHz	160 MHz[c]
Projected baseline lengths	10–240 m	13–162 m
Phase and amplitude calibrator	0528 + 134 (5.7 Jy)[d]	0528+134 (4.2 Jy and 5.7 Jy)[e]
Passband calibrator	3C 273 and noise source	3C 454.3
Beam size (for continuum)	2.″6 × 2.″0[f]	13″ × 6.″1[f, g]
Beam size (for line)	2.″6 × 2.″0 (^{13}CO)[f] and 3.″9 × 3.″1 (C^{18}O)[h]	6.″6 × 4.″7[f]
Noise level (for continuum)	0.7 mJy beam^{-1}	6.7 mJy beam^{-1}
Noise level (for line)	0.7 K (^{13}CO) and 0.4 K (C^{18}O)	0.5 K

[a] Only 4 antennas were available in 1993 December because of mechanical problems.

[b] Measured at the zenith.

[c] Bandwidth was 80 MHz in 1995 February.

[d] This was estimated from observations of Uranus (primary calibrator) and 3C 273 (secondary calibrator) by assuming that the brightness temperature of Uranus is 130 K.

[e] These were measured in 1993 December and 1995 February, respectively, based on observations of Uranus on the assumptions of its brightness temperature of 130 K.

[f] Natural weight was applied to the *u-v* data.

[g] Only those data taken in 1993 with the compact configuration D were used because the data taken in 1995 had poor sensitivity to continuum due to the narrow bandwidth for the continuum observations.

[h] Natural weight and a 60 kλ taper were applied to the *u-v* data to improve signal-to-noise ratio.

the origin of the rotation in detail in this paper. Combining the new specific angular momentum results with those for three previously observed infalling envelopes and two T Tauri gas disks, we find that specific angular momenta take a relatively constant value over the radius range 200–2000 AU (0.001–0.01 pc). This is in contrast to the accepted relation between core size and angular momentum for dense cores on scales of 0.03–0.4 pc, 6000–80,000 AU (Goodman et al. 1993). We will consider possible reasons for these results.

2. OBSERVATIONS

Observations of I04169 were made using the Owens Valley Radio Observatory (OVRO) millimeter-wave array. We observed ^{13}CO $J = 1$–0, C^{18}O $J = 1$–0, and 2.7 mm continuum emission simultaneously. Spectral information was obtained using a digital correlator with a velocity resolution of 0.34 km s^{-1} for each line, while a single-channel analog correlator with a 1 GHz bandwidth was employed for the simultaneous continuum observations. These observations are insensitive to structures extended more than $\sim 56''$.

Observations of I04365 were made using the Nobeyama Millimeter Array (NMA) at Nobeyama Radio Observatory.[7] ^{13}CO $J = 1$–0 and 2.7 mm continuum emission were simultaneously observed with the digital spectrocorrelator FX, covering a total bandwidth of 160 MHz with 1024 spectral channels. This resulted in a velocity resolution of 0.43 km s^{-1} at the ^{13}CO line frequency. The 2.7 mm continuum data were derived by averaging line-free channels of the FX data. Structures extended by more than $\sim 43''$ are not detectable in these observations.

Table 1 summarizes observing periods, receivers and their sensitivities, visibility calibrators and their fluxes, synthesized beam sizes, noise levels, and other details of the observations. After calibrating *u-v* data and making dirty maps, we CLEANed spectral channel maps and 2.7 mm continuum maps using the Astronomical Image Processing System (AIPS). Integrated intensity maps for the spectral line emission were made by summing the channel maps.

3. RESULTS

3.1. *The 2.7 millimeter Continuum Emission*

Continuum emission at $\lambda = 2.7$ mm was detected from both I04169 and I04365 with total flux densities of 17 ± 0.7 and 59 ± 6.7 mJy, respectively. Neither source was resolved at the angular resolutions employed (2.″6 × 2.″0 for I04169 and 13″ × 6.″1 for I04365). We list peak positions and total flux densities in Table 2. These flux densities are consistent with those expected at 2.7 mm, following the power-law spectral energy distributions derived from their submillimeter fluxes, with spectral indices of 3.0 for I04169 and 2.6 for I04365 (see Moriarty-Schieven et al. 1994), suggesting that the 2.7 mm continuum emission originates from warm dust. The emission peak of I04365 is spatially coincident with previous interferometric measurements (Terebey, Chandler, & André 1993; Ohashi et al. 1996b). Accordingly, we assume that our peak position is that of the central star. We make the same assumption for I04169, for which no previous interferometric continuum measurements have been published.

[7] Nobeyama Radio Observatory (NRO) is a branch of the National Astronomical Observatory, an interuniversity research institute operated by the Ministry of Education, Science, Sports, and Culture of Japan.

TABLE 2

PHYSICAL PARAMETERS DERIVED FROM CONTINUUM EMISSION

SOURCE	PEAK POSITION R.A. (1950)	PEAK POSITION decl. (1950)	FLUX DENSITY (mJy)	MASS ($M_\odot$)
IRAS 04169+2702.....	4 16 53.8	27 02 48	17 ± 0.7	2.8×10^{-2}
IRAS 04365+2535.....	4 36 31.3	25 35 56	59 ± 6.7	9.8×10^{-2}

NOTES.—Units of right ascension are hours, minutes, and seconds, and units of declination are degrees, arcminutes, and arcseconds. In deriving total mass (gas + dust) from the flux density, we adopted a mass opacity of 5.5×10^{-3} cm^2 g^{-1} at $\lambda = 2.7$ mm, which was estimated from the mass opacity at $\lambda = 400$ μm (Keene, Hildebrand, & Whitcomb 1982) by assuming its power-law dependence on λ with the index of 1. We also assumed the dust temperature of 30 K. Details of the mass derivation were described in Ohashi et al. 1991, 1996b.

The total mass (gas + dust) of each continuum source was estimated by assuming optically thin continuum emission and standard dust propertes (see Ohashi et al. 1991), and is given in Table 2. The angular resolution of the I04169 map, 2.″6 × 2.″0, equivalent to 360 AU × 280 AU at the 140 pc distance to the Taurus molecular cloud (Elias 1978), implies a compact dust source with a radius of $\lesssim$150 AU. This is similar to the size of disks found around other embedded stars, such as L1551 IRS 5 (Lay et al. 1994; Looney, Mundy, & Welch 1997), and suggests the presence of a circumstellar disk. For I04365, our beam size of 13″ × 6″ is much lager than the typical size of a compact dust disk, so that significant emission may derive from an extended envelope.

3.2. *Line Emission*

3.2.1. *IRAS 04169 + 2702*

For I04169, emission in the ^{13}CO $J = 1$–0 line was detected between $V_{LSR} = 4.8$ and 8.9 km s^{-1}, with a sensitivity of $\sim$0.7 K (1 σ level) at 2.″6 × 2.″0 resolution, while C^{18}O $J = 1$–0 was detected in a narrower velocity range between $V_{LSR} = 5.8$ and 7.9 km s^{-1}, with a sensitivity of $\sim$0.4 K (1 σ level) at 3.″9 × 3.″1 resolution. The ^{13}CO emission appears to arise from gas in both the envelope and the outflow, and is therefore not suitable for studying the kinematics of the envelopes (see Appendix A). Only the C^{18}O data for I04169 are used in this paper.

Figure 1*a* (Plate 9) shows the total intensity map of C^{18}O integrated over the detected velocity range and superimposed on the outflow map obtained with the NMA (Tamura et al. 1997). We can see a structure elongated in the northwest-southeast direction (P.A. 154°), centered on the 2.7 mm continuum peak (see § 3.1) and perpendicular to the outflow axis. The deconvolved size of this structure is 16″ × 8.″0, corresponding to 2200 AU × 1100 AU. Double intensity peaks are evident, the stronger being located at $\sim$2″ north of the central star. A velocity gradient along the major axis is seen in the mean velocity map of Figure 1*b*. With respect to the systemic velocity of $\sim$6.8 km s^{-1} measured at $\sim$17″ resolution in C^{18}O $J = 1$–0 with the Nobeyama 45 m telescope (N. Ohashi, unpublished data),[8] the C^{18}O emission in the northwest is redshifted, with mean velocities more than 7 km s^{-1}, while to the southeast it is blueshifted, with the mean velocities less than 6.5 km s^{-1}. The velocity channel maps in Figure 2 demonstrate that the C^{18}O emission is detected at the southeast of the central star in the blueshifted velocity channels at $V_{LSR} = 6.0$, 6.3, and 6.7 km s^{-1}, while it is confined on the opposite side at redshifted velocities 7.0, 7.4, and 7.7 km s^{-1}, as in the mean velocity map (Fig. 1*b*). There is no evidence for a systematic velocity gradient along the minor axis of the elongated structure.

The double-peaked, elongated structure of C^{18}O perpendicular to the outflow axis, with its relatively simple kinematics compared to that of ^{13}CO (Appendix A), leads us to the conclusion that, for the most part, the C^{18}O emission arises from a rotating disk or flattened envelope (hereafter simply called a flattened envelope). The deconvolved radius and inclination angle of this flattened envelope are 1100 AU and 60° (0° for face-on), respectively. The velocity gradient along its major axis (A-A′ in Fig. 1*b*) is clearly identified in the position-velocity diagram of Figure 3*a*. This velocity gradient is nearly symmetric with respect to the central stellar position, as well as with respect to the systemic velocity of $\sim$6.8 km s^{-1}, as would be expected for a rotating flattened envelope around I04169. The rotation velocity is estimated to be $\sim$0.23 km s^{-1} at a radius of 370 AU after correction for the inclination of 60°.

This evidence of rotation does not rule out the possibility that the flattened envelope is also infalling. High-resolution observations of HL Tau (Hayashi et al. 1993), L1551 IRS 5 (Ohashi et al. 1996a), and IRAS 04368+2557 (Ohashi et al. 1997) have revealed that the kinematics of $\sim$1000 AU envelopes are dominated by dynamical infall although they also show rotation. When a disk is not completely edge-on, the signature of infall appears as a velocity gradient along the disk minor axis. However, Fig. 3*b* shows that no such velocity gradient is apparent along the minor axis (B-B′ in Fig. 1*b*) of the I04169 flattened envelope.

As a result, additional radial motion in the flattened envelope around I04169 seems unlikely. Nonetheless, we believe that there is also infall (see also § 4.1); for pure rotation, blueshifted emission will be observed only at one side of the disk with respect to its minor axis, while redshifted emission will appear only at the other side. The individual channel maps of I04169 in Figure 2 show that there are weak blueshifted features in the northwest where the redshifted emission dominates ($V_{LSR} = 6.7$ km s^{-1}), and weak redshifted emission to the southeast where the blueshifted emission is strong ($V_{LSR} = 7.0$ km s^{-1}). This is similar to the

[8] LSR velocities measured with the 45 m telescope and interferometer at NRO were shifted by ~ -0.27 km s^{-1} for the Taurus region from those measured at other radio observatories since 1990 December, because in calculating LSR velocities NRO assumed a basic solar motion slightly different from the conventional definition. In this paper, we corrected the LSR velocities of the data taken at NRO for consistency with data taken at other observatories.

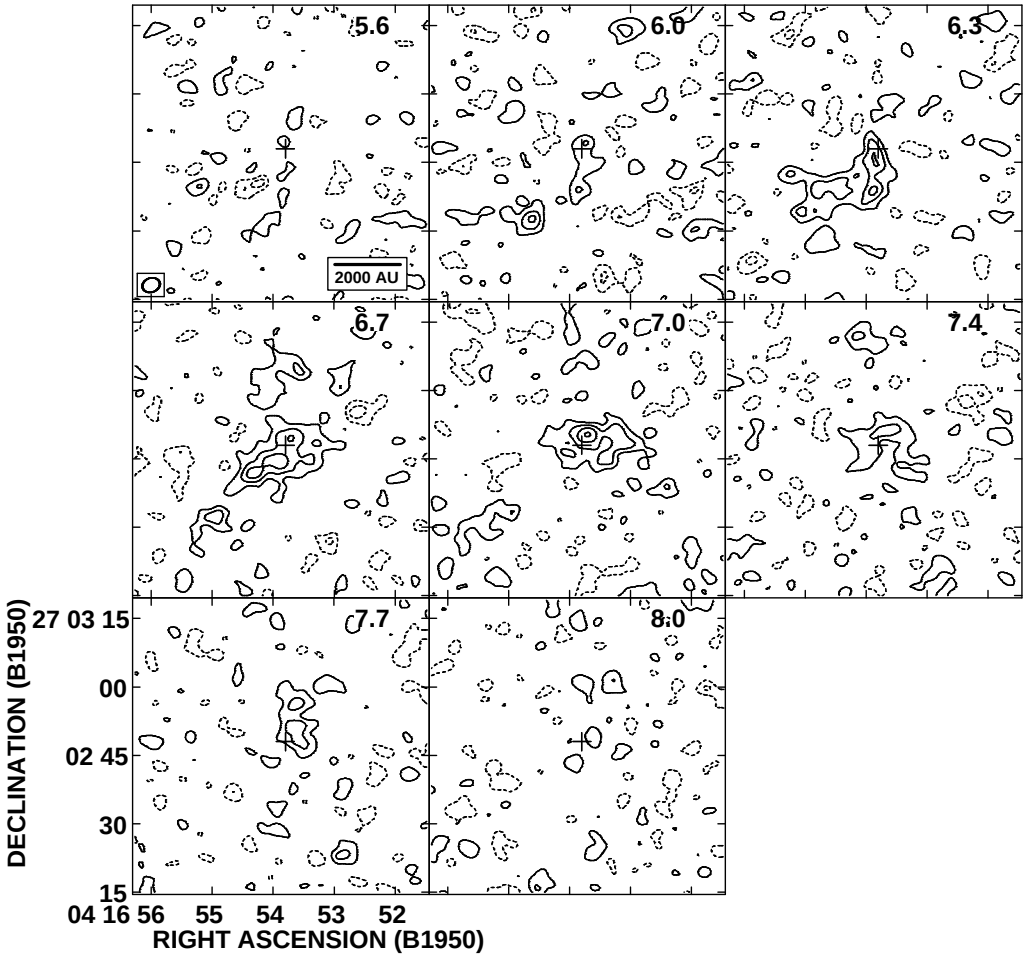

FIG. 2.—$C^{18}O$ channel maps of IRAS 04169+2702 with a velocity resolution of 0.34 km s^{-1}. The central LSR velocity of each velocity channel is denoted at the top right corner in each corresponding panel. The systemic velocity is $\sim$6.8 km s^{-1}. Contours are drawn at 1.5 σ steps from the 1.5 σ level (*solid contours*) and at -1.5 σ step from the -1.5 σ level (*dashed contours*). The 1 σ level corresponds to $\sim$50 mJy $beam^{-1}$ or 0.4 K in brightness. The cross in each panel indicates the position of the central star.

case of IRAS 04368+2557, where both infall and rotation motions are observed (Ohashi et al. 1997).

The total integrated intensity of the $C^{18}O$ flattened envelope was 2.2 ± 0.2 Jy km s^{-1} (integrated above the 2 σ level), which corresponds to a total gas mass of 0.024 $M_\odot$, assuming $T_{ex} = 30$ K and optically thin $C^{18}O$ emission (see Ohashi et al. 1997 for details of the mass estimation).

3.2.2. *IRAS 04365 + 2535*

The ^{13}CO $J = 1$–0 emission was detected from I04365 at velocities between $V_{LSR} = 4.8$ and 7.8 km s^{-1}, except for the channel centered at $V_{LSR} = 6.3$ km s^{-1}, close to the systemic velocity of $\sim$6.4 km s^{-1} (see Ohashi et al. 1996b).[9] The angular resolution was $6''.6 \times 4''.7$, and the sensitivity was $\sim$0.5 K (1 σ level). Figure 1*c* shows the total intensity map integrated over the above velocity range, superimposed on the molecular outflow observed with the NMA (Tamura et al. 1996) The well-defined emission peak is shifted to the southeast of the continuum peak by $\sim 2''$, with weaker features extending to the north, west, and slightly to the south of the peak. The size of the condensation is $\sim 10''$ or 1400 AU (FWHM). The fainter features elongated to the north and to the south are spatially correlated with the blueshifted and redshifted outflow lobes, respectively, suggesting that these fainter features are part of the outflow.

In the mean velocity map of ^{13}CO presented in Figure 1*d*, the northeastern part of the condensation is blueshifted while the southwestern part is redshifted with respect to the systemic velocity. The velocity gradient is hence from northeast to southwest, and roughly perpendicular to the outflow. The ^{13}CO velocity channel maps in Figure 4, which confirm the velocity gradient, display a sudden spatial variation at the systemic velocity; the emission arises only from the east of the central star at blueshifted velocities ($V_{LSR} = 5.0$, 5.5, and 5.9 km s^{-1}), and only from the southwest at redshifted velocities ($V_{LSR} = 6.7$, 7.2, and 7.6 km s^{-1}). Although the emission at each velocity is elongated from north to south or from northwest to southeast, the direction of the outflow, and may be partly attributable to the outflow, the dominant velocity gradient is from northeast to southwest and cannot result from outflowing motion.

The relatively compact condensation centered close to I04365, which shows an abrupt velocity discontinuity perpendicular to the outflow axis, is most naturally interpreted as a rotating circumstellar disk or flattened envelope. This condensation was previously detected in CS $J = 2$–1 with

[9] See footnote 8.

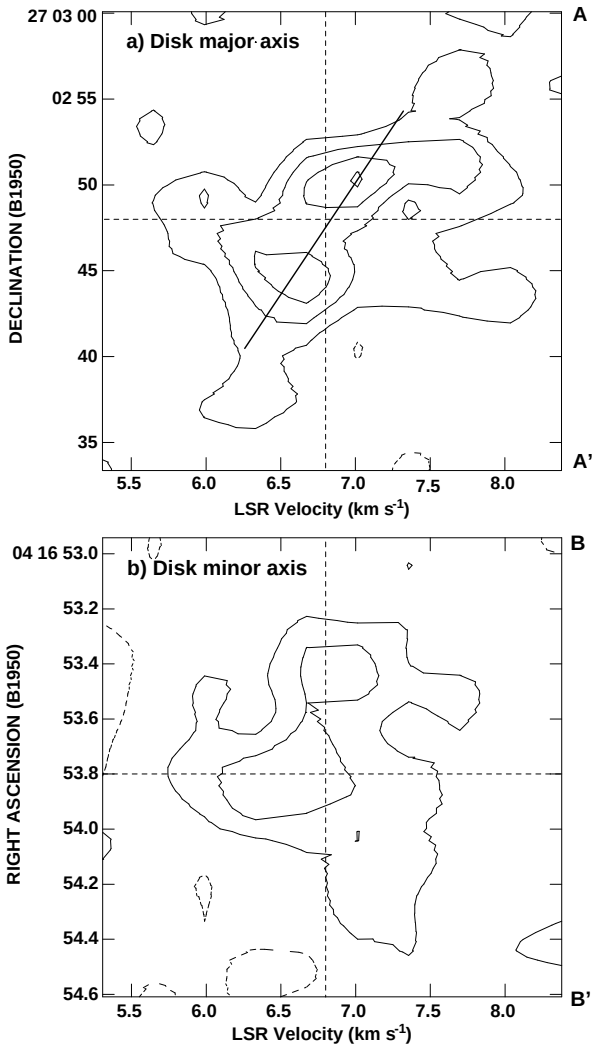

FIG. 3.—Position-velocity diagrams of the $C^{18}O$ elongated structure around IRAS 04169+2702. The contours are drawn in the same manner as in Fig. 2. The vertical and horizontal dashed lines indicate the systemic velocity and the position of the central star, respectively. (*a*) Position-velocity diagram along the major axis of the elongated structure (the line A-A′ with P.A. = 154° in Fig. 1*b*). The orientation of the velocity gradient is shown by the thick line. (*b*) Same as (*a*), but along the minor axis of the elongated structure (the line B-B′ with P.A. = 64° in Fig. 1*b*).

size 1500 AU × 1500 AU, using the NMA (Ohashi et al. 1996b). Although it could be argued that the compact structure results from insufficient sensitivity to more extended emission arising from the large molecular cloud core, L1534, it is unlikely that we would fail to detect structures smaller than ∼43″ (see § 2), which is significantly larger than the size of the compact structure. In addition, the sharp velocity gradient cannot be produced by insufficient *u-v* coverage problems. We therefore believe that the compact rotating condensation represents the inner part of the L1534 dense core.

It should be acknowledged that the compact condensation does not show any flattened or disklike morphology perpendicular to the outflow axis; rather, at the half-maximum contour level, the emission appears round, although an associated infrared reflection nebula could imply a nonspherical circumstellar envelope (Tamura et al. 1996). The absence of a disklike structure could be due to insufficient spatial resolution, confusion with the outflow, since ^{13}CO is likely to be optically thick, or even a relatively low inclination angle of the disk, which is estimated to be 40°–60° (0° for face-on) from the inclination angle of the outflow (Chandler et al. 1996).

Figure 5*a*, the position-velocity diagram through the I04365 central star position at P.A. 70° (A-A′ in Fig. 1*d*), shows a clear velocity gradient perpendicular to the outflow axis. The rotational velocity is ~ 0.87 km s^{-1} at 580 AU radius, assuming an underlying disk structure with an inclination angle of 50°. Because the northeastern part is blueshifted with respect to the systemic velocity and the opposite part is redshifted, the rotation is clockwise as viewed from the southeast side of the disk. In contrast, the L1534 dense core (TMC-1A), which surrounds I04365, shows an opposite velocity gradient on a larger, 0.1 pc scale (Goodman et al. 1993). If the velocity gradient on the large scale also originates from rotation, then rotational direction is different for different scale lengths. A similar inconsistency was also found for IRAS 04368+2557 (Ohashi et al. 1997).

Figure 5*b* presents the position-velocity diagram along the outflow axis across the central star (B-B′ in Fig. 1*d*). A small velocity gradient, redshifted to the south and blueshifted to the north like the outflow, can be recognized, and, as noted before, the faint extended features to the north and to the south from the central peak are spatially correlated with the ^{12}CO outflow lobes (see Fig. 1*c*). Thus, the gradient may be due to outflow gas contaminating the ^{13}CO velocity field. Such a velocity gradient would also be expected if the disk were infalling, as in the cases of HL Tau and L1551 IRS 5, but there is insufficient evidence to make that case here (see also § 4.1).

The total integrated intensity of the ^{13}CO emission was 4.3 ± 0.5 Jy km s^{-1} (integrated above the 2 σ level), which corresponds to a total gas mass of 8.3×10^{-3} $M_\odot$, assuming $T_{ex} = 30$ K and optically thin ^{13}CO emission (see Ohashi et al. 1997 for details of the mass derivation). This provides a lower limit to the mass of the envelope, since the ^{13}CO emission from the envelope is likely to be optically thick.

4. DISCUSSION

4.1. *Nature of Rotation*

From the present observations, the circumstellar envelopes (or disks) around I04169 and I04365 appear to be rotating. Physical properties of the rotating envelopes are summarized in Table 3, together with those of infalling envelopes around three embedded sources, HL Tau, L1551 IRS 5, and IRAS 04368+2557, and those of two gaseous disks around T Tauri stars, GG Tau[10] and DM Tau (see references in Table 3). Evidently, rotation around young stellar objects can be divided into two types, either rotationally supported disks, probably in Keplerian motion around visible T Tauri stars, such as that around GG Tau (Kawabe et al. 1993; Dutrey, Guilloteau, & Simon 1994), or infalling flattened envelopes with non-Keplerian rotation around embedded sources, such as that around HL Tau (Hayashi et al. 1993). In centrifugally supported disks the rotational velocity is given by $(GM_R/R)^{1/2}$, where G is the gravitational constant and M_R is the mass contained within the radial

[10] The disk around GG Tau has a ring structure (Dutrey, Guilloteau, & Simon 1994).

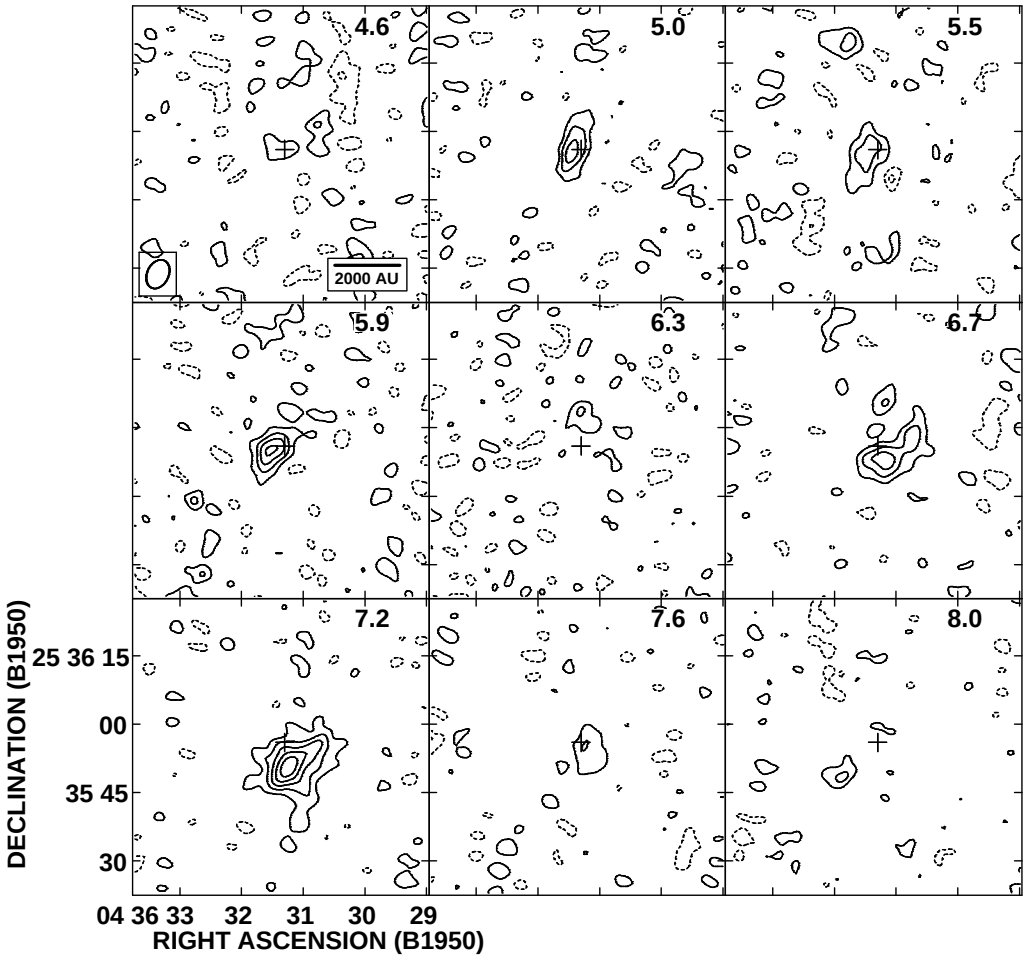

FIG. 4.—^{13}CO channel maps of IRAS 04365+2535 with a velocity resolution of 0.43 km s^{-1}. The central LSR velocity of each velocity channel is denoted at the top right corner in each corresponding panel. The systemic velocity is ~6.4 km s^{-1}. Contours are drawn at 1.5 σ steps from the 1.5 σ level (*solid contours*) and at −1.5 σ step from the −1.5 σ level (*dashed contours*). The 1 σ level corresponds to ~170 mJy beam^{-1} or 0.5 K in brightness. The cross in each panel indicates the position of the central star.

TABLE 3

PHYSICAL PROPERTIES OF INFALLING ENVELOPES AND ROTATING DISKS AROUND EMBEDDED SOURCES AND T TAURI STARS IN TAURUS

Source	Type[a]	R[b] (AU)	M[c] ($M_\odot$)	R_{rot}[d] (AU)	V_{rot}[e] (km s^{-1})	j[f] (km s^{-1} pc)	Reference
IRAS 04169+2702.....	I (?)	1100	2.4×10^{-2}	370	0.23	4.3×10^{-4}	1
IRAS 04365+2535.....	R	700	$\geq 8.3 \times 10^{-3}$	580	0.87	2.5×10^{-3}	1
HL Tau	I	1400	3.0×10^{-2}	700	0.20	7.0×10^{-4}	2
L1551 IRS 5	I	2800	2.7×10^{-1}	900	0.23	1.0×10^{-3}	3
IRAS 04368+2557.....	I	2000	3.8×10^{-2}	2000	0.05	5.0×10^{-4}	4
GG Tau.....	R	800	1.3×10^{-3}	200	1.60	1.6×10^{-3}	5
DM Tau	R	830	2.3×10^{-3}	350	0.93	1.6×10^{-3}	6

[a] Type of rotation. R = Rotationally supported; I = Infalling.
[b] Radius.
[c] Total mass.
[d] Radius at which rotation was measured.
[e] Rotational velocity at R_{rot}.
[f] Local specific angular momentum.

NOTE.—R_{rot} and V_{rot} of each source were estimated from position-velocity diagrams cutting along the major axes of the disks or envelopes except for I04368+2557, for which the two parameters were derived using a model (see Ohashi et al. 1997). In the case of GG Tau and DM Tau, the two parameters were estimated by ourselves from the position-velocity diagrams in the reference papers. Local specific angular momenta were simply calculated by $j = R_{rot} V_{rot}$.

REFERENCES.—(1) This work; (2) Hayashi et al. 1993; (3) Saito et al. 1996; (4) Ohashi et al. 1997; (5) Dutray et al. 1994; (6) Saito et al. 1995.

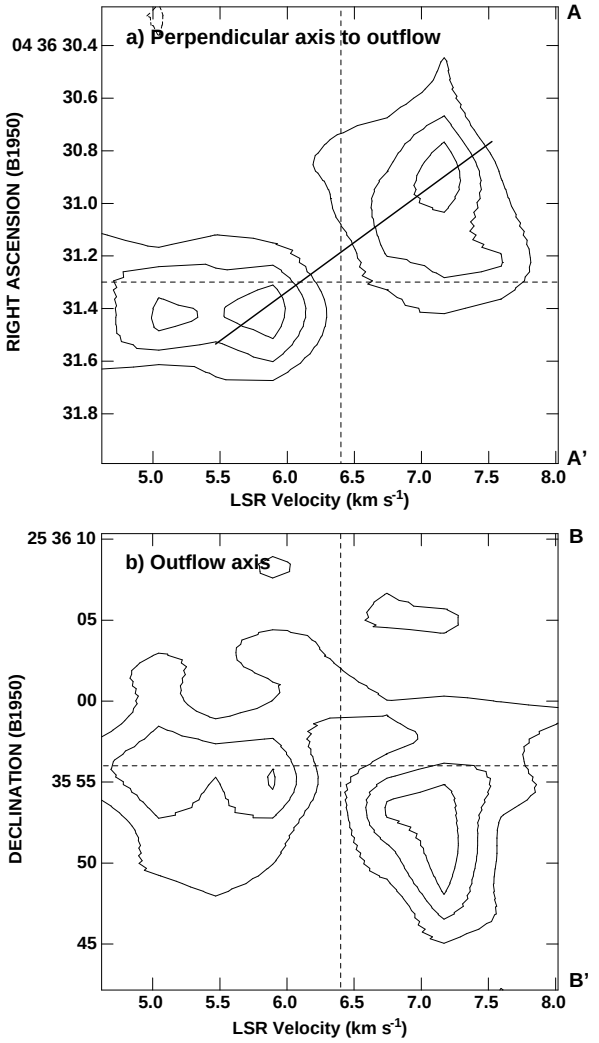

FIG. 5.—Position-velocity diagram of the ^{13}CO envelope around IRAS 04365+2535. The contours are drawn in the same manner as in Fig. 4, and two dashed lines have the same meanings as in Fig. 2. (*a*) Diagram along the direction perpendicular to the outflow axis (the line A-A′ with P.A. = 70°). The velocity gradient is represented by the thick line. (*b*) Diagram along the outflow axis (the line B-B′ with P.A. = −20).

distance R. In radially infalling envelopes with rotation, the rotational speed is smaller than the value derived from $(GM_R/R)^{1/2}$. How do these arguments apply to I04169 and I04365?

In § 3.2.1 we pointed out the possibility that the I04169 envelope is infalling as well as rotating. If the velocity field is purely rotational, the rotational velocity of 0.23 km s^{-1} (corrected for the inclination angle of 60°) at a radius of 370 AU requires a dynamical mass of only $\sim 0.02\ M_\odot$ within this radius. This value is comparable to the mass derived for the C^{18}O flattened envelope, $0.024\ M_\odot$ (see § 3.2.1), and for the inner compact dust disk, $0.03\ M_\odot$ (see § 3.1). However, unless I04169 is an extremely young protostar, its protostellar core mass cannot be much smaller than the typical T Tauri mass of $\sim 0.5\ M_\odot$ in Taurus. Quantitative arguments in Appendix B suggest that a stellar mass of $\sim 0.1\ M_\odot$ is plausible, assuming an age of 10^5 yr. We therefore suggest that there must be infalling motion as well as rotation in the flattened envelope associated with I04169. This result is consistent with the spectral energy distribution of I04169, which is well explained by a model of an infalling envelope (Kenyon et al. 1993).

In contrast to the flattened envelope around I04169, the envelope around I04365 rotates rapidly: its rotational velocity is 0.87 km s^{-1} (corrected for the inclination angle of 50°) at radius 580 AU. This is similar to the values found for material orbiting T Tauri stars (see Table 3), and requires a binding mass of $\sim 0.5\ M_\odot$ within the 580 AU radius, or $\sim 0.4\ M_\odot$ if we adopt an inclination angle of 60° instead of 50°. The bolometric luminosity of I04365, $2.4\ L_\odot$ (Myers et al. 1987), implies a central stellar mass of $0.17\ M_\odot$, assuming an age of 10^5 yr (see Appendix B), while the mass of the central condensation is $\sim 0.1\ M_\odot$ (see § 3.1) from the continuum observations. The good agreement between the total measured mass and the dynamical mass within 580 AU is therefore consistent with a rotationally supported disk.

Theoretical fits to the spectral energy distribution of I04365 suggest that this source is surrounded by infalling material (e.g., Adams, Lada, & Shu 1987; Kenyon et al. 1993). According to Kenyon et al., the mass infall rate in the envelope around I04365 would be $7.8 \times 10^{-6}\ M_\odot$ yr^{-1}, assuming the stellar mass to be $0.17\ M_\odot$ (see above). For this infall rate in the envelope, the radial velocity, V_i, can be estimated from $V_i = \dot{M}R/M$, where $\dot{M}$ is the mass infall rate, M the mass of the envelope, and R its radius (Ohashi et al. 1996a). When $M = 0.1\ M_\odot$ (see § 3.1) and $R = 700$ AU (see Table 3), V_i is 0.27 km s^{-1} at 700 AU radius. With an envelope inclination angle of 50°, the observable radial velocity would be 0.21 km s^{-1}. This radial velocity is not large enough to be directly detected with the present velocity resolution of 0.43 km s^{-1} (see Table 1). More important, since it is considerably smaller than the rotational velocity of the envelope, the envelope may be predominantly rotationally supported.

4.2. *Size Dependence of Specific Angular Momentum*

As shown in Table 3, the two T Tauri stars and probably I04365 have rotationally supported disks with radii less than 1000 AU, while all embedded protostars except I04365 have infalling envelopes with radii larger than 1000 AU. The embedded protostars with infalling envelopes have smaller dust condensations, but their masses may be smaller than those of compact disks around T Tauri stars (Ohashi et al. 1991, 1996b). According to the scenario in which an embedded protostar evolves into a visible T Tauri star, gas in a flattened infalling envelope accumulates onto a smaller rotationally supported disk. In this case, the size scale of rotationally supported disks is determined by the specific angular momenta of infalling envelopes. It is thus interesting to ask how the specific angular momenta of the infalling envelopes are initially set, since this physical process will determine the size of protoplanetary disks in which planetary system formation could proceed.

Among the sources listed in Table 3, large-scale rotation has been observed around IRAS 04368+2557 (hereafter I04368) and I04365. For I04368, the specific angular momentum of the flattened infalling envelope with a 2000 AU (0.01 pc) radius is more than 1 order of magnitude smaller than that of the surrounding L1527 cloud core with radius 0.08 pc (Ohashi et al. 1997). Similarly, for I04365 the specific angular momentum of the ^{13}CO rotating envelope at a radius of 580 AU (0.003 pc) is also an order of magnitude smaller than that of the surrounding L1534 dense core

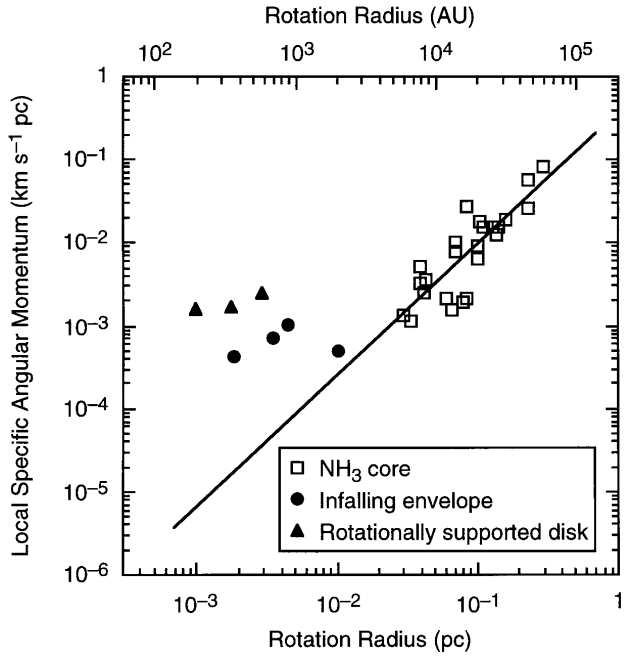

FIG. 6.—Local specific angular momentum plotted as a function of the rotation radius. Open squares, filled circles, and filled triangles represent data for NH_3 cores (Goodman et al. 1993), infalling envelopes and rotationally supported disks, respectively. The solid line indicates a power-law relation with an index of 1.6 for the NH_3 cores (cf. Goodman et al. 1993).

(TMC-1A) at a radius of 0.14 pc (Goodman et al. 1993). These two examples suggest that the specific angular momentum of a gas element in a star-forming dense core is largely dependent on the distance from the central star.

In order to illustrate the variation of angular momentum with radius, in Figure 6 we compare the local specific angular momenta of the objects in Table 3 with those of dense cores compiled by Goodman et al. (1993). We use local specific angular momentum because it is simply and uniquely given by $V_{\rm rot} R_{\rm rot}$, where $V_{\rm rot}$ is the rotational velocity corrected for inclination at the radius $R_{\rm rot}$, without any assumptions about mass and velocity distributions as a function of radius. For this purpose we multiplied the "mean" specific angular momenta derived by Goodman et al. (1993) by $\frac{5}{8}$.[11]

Figure 6 shows that while the local specific angular momentum for dense cores systematically varies with radius, it is almost constant for infalling envelopes and rotationally supported disks. For radii between 0.03 and 0.4 pc (6000–80,000 AU), the local specific angular momentum ranges from $\sim 10^{-3}$ to $\sim 10^{-1}$ km s^{-1} pc. As noted by Goodman et al. (1993), the dependence on radius is well fitted by a power law with an index of ~ 1.6 (see also Goldsmith & Arquila 1986). By contrast, the specific angular momenta of infalling envelopes and rotationally supported disks are much smaller, and remain almost constant at $\sim 10^{-3}$ km s^{-1} pc over the radius range 0.001–0.01 pc (200–2000 AU). However, this value is much larger than would be anticipated from an extrapolation of the power-law relation to smaller radii. Clearly the size dependence of local specific angular momentum changes between the large scales of dense cores and the smaller scale envelopes and disks.

Figure 6 suggests that a star-forming dense core can be divided into two zones based on the size dependence of local specific angular momentum; an inner region, where gas has relatively constant specific angular momentum, and an outer region, where the power-law relation applies. These two zones are obvious in the cases of I04365 (L1534) and I04368 (L1527); the data points for the infalling envelope/disk and for the corresponding dense core fall on the curve as appropriate. Of course, Figure 6, being a compilation of rotational data for dense cores, infalling envelopes, and rotationally supported disks with various radii ranging from 0.001 to 0.4 pc, does not in itself define a distribution of local specific angular momentum in a star-forming dense core. Nevertheless, the above two examples suggest that it may be regarded as approximating the distribution of specific angular momentum in a star-forming dense core, which generally has two zones. From Figure 6, the two regions are divided at roughly ~ 0.03 pc (6000 AU); there the power-law relation for local specific angular momentum extrapolated from larger scales intersects the value of $\sim 10^{-3}$ km s^{-1} pc, the typical specific angular momentum of infalling envelopes and rotationally supported disks.

4.3. *Size Scale for Dynamical Collapse*

The above arguments suggest that at radii smaller than the scale of ~ 0.03 pc, a gas element in a star-forming core retains a constant specific angular momentum of 10^{-3} km s^{-1} pc, the typical value for infalling envelopes and rotationally supported disks. Given that local specific angular momentum is conserved within ~ 0.03 pc, this characterizes the size scale for dynamical collapse.

It is ineresting to note that the size scale of 0.03 pc encloses a typical stellar mass in Taurus. For a dense core supported by thermal pressure at $T = 10$ K, the critical mean density is $\sim 10^5$ cm^{-3} at radius 0.03 pc (Myers, Linke, & Benson 1983; Bonner 1956). At the same radius these parameters give a critical mass of $\sim 0.6\ M_\odot$, typical of the mass of T Tauri stars associated with the Taurus molecular cloud. Although nonthermal pressure may play an important role in support of dense cores, its contribution may be much smaller than that of thermal pressure at the radius 0.03 pc (see § 4.4).

The region outside the radius 0.03 pc of a star-forming dense core is most probably in virial equilibrium. There, the local specific angular momentum is proportional to $R^{1.6}$, which can be explained if a dense core is in virial equilibrium with the line width roughly proportional to $R^{0.5}$ and if the ratio β of rotational to gravitational energies is independent of R (Goodman et al. 1993). In addition, if a gas element in this outer region is undergoing dynamical collapse toward the central star, it would eventually violate the power-law relation as a result of angular momentum conservation. Finally, the dense cores in the list compiled by Goodman et al. (1993) are not necessarily associated with central infrared sources, suggesting that the power-law relation for specific angular momentum is independent of the existence of central embedded sources. These arguments suggest that the power-law relation is intrinsic to dense cores and is not directly related to star-forming activities, such as dynamical infall, and that the outer region seems to be in virial equilibrium. We note, however, that we cannot

[11] Goodman et al. (1993) calculated specific angular momenta of NH_3 cores by a formula $\frac{2}{5}\omega_d d^2$, where d is the diameter of each core at the FWHM level and ω_d is the angular velocity (velocity gradient) measured over d. We define the local specific angular momentum as $V_{\rm rot} R_{\rm rot} = (\omega_d d/2)(d/2) = \omega_d d^2/4$, which is $\frac{5}{8}$ of their definition.

rule out the possibility that the outer region, following the power-law relation, independently and locally undergoes dynamical collapse to fragment and to form another condensation or a star that carries most of the original angular momentum as an orbital motion.

In contrast, a low-mass star-forming dense core is undergoing dynamical collapse inside the radius of ~ 0.03 pc. In dynamically collapsing regions, local specific angular momentum is independent of radius because of angular momentum conservation. The important point is that the observed infalling envelopes and rotationally supported disks have the same value of $\sim 10^{-3}$ km s^{-1} pc.[12] Note that the local specific angular momentum for each rotationally supported disk listed in Table 3 should be comparable to that previously carried by the infalling envelope, if it was measured at the outermost radii (Lin et al. 1994). Figure 6 suggests that gas elements in dynamically infalling regions have a typical specific angular momentum of $\sim 10^{-3}$ km s^{-1} pc. This typical specific angular momentum in infalling regions eventually determines the size of the rotationally supported disks that form at the centers of the envelopes. The value 10^{-3} km s^{-1} pc leads to ~ 50 AU for the radius of a rotationally supported, non–self-gravitating disk around a central star with a mass of 1 $M_\odot$. This radius is in good agreement with the size of compact disks observed in dust emission around T Tauri stars and embedded sources (Beckwith et al. 1990; Lay et al. 1994; Mundy et al. 1996; Kitamura, Kawabe, & Saito 1996; Wilner, Ho, & Rodríguez 1996; Looney et al. 1997).

What is the physical reason for the infalling envelopes and rotationally supported disks having similar specific angular momenta? Suppose the angular momentum distribution of pre–star-forming dense cores, from which the seven sources formed, is consistent with the power-law relation. If a dynamically collapsing region of a dense core has a radius of ~ 0.03 pc and is limited to only within this radius, then the specific angular momentum of a gas element in the infalling region will automatically be set to $\sim 10^{-3}$ km s^{-1} pc, the largest specific angular momentum carried by the outermost gas element in the infalling region. Thus the similar specific angular momentum among the seven sources suggests that there may be a physical basis for dynamical collapse occurring only at the scale of ~ 0.03 pc in the Taurus molecular cloud.

4.4. *Possible Origins of the Size Scale for Dynamical Collapse*

A simple explanation for the size scale of ~ 0.03 pc relies on the Jeans length $\lambda_J = (\pi kT/G\mu\rho)^{1/2}$, where k, T, G, μ, ρ are respectively Boltzmann's constant, gas kinetic temperature, the gravitational constant, mean molecular weight per hydrogen atom, and mass density. A gas cloud with molecular hydrogen density of 10^5 cm^{-3} at 10 K is gravitationally unstable to perturbations longer than $\lambda_J = 0.07$ pc, similar to the derived scale for dynamical collapse. However, this naive argument cannot physically justify the present case, because the Jeans length originally provides the smallest scale for dynamically unstable regions and because, unless the gas has two-dimensional (plane) or one-dimensional (filament) morphology, the perturbation growth rate is larger for longer scale lengths (Larson 1985); a more or less spherical molecular cloud core would collapse at once. We must therefore find another answer to the question of why only gas within the radius of ~ 0.03 pc appears to be undergoing infall while the remainder on larger scales is dynamically stable.

There are two possible explanations, either inside-out collapse (Shu 1977) or small nonthermal motions on smaller scales. In the case of inside-out collapse, a dynamically infalling region is confined inside the expansion wave front in a star-forming dense core. The expansion wave can reach a radius comparable to the Jeans length, the sound speed multiplied by the free-fall timescale, which is roughly the lifetime of accreting protostars, $\sim 10^5$ yr (Myers et al. 1987; Kenyon 1990). If, however, the expansion wave propagates further, a region entering the expansion front will collapse by losing thermal pressure to sustain that region against gravity. Thus, for the inside-out collapse scenario to be consistent with the present results, another mechanism, such as outflow, must be invoked to stop the dynamical collapse when the expansion wave reaches the distance of ~ 0.03 pc from the central protostar.

Alternatively, nonthermal motions may play a critical role in setting the size scale for dynamical collapse. Goodman et al. (1993) suggested that the power-law relation for dense cores is connected with Larson's size–line width relation, $\Delta V = 1.2R^{0.4-0.5}$, where ΔV is the velocity dispersion in km s^{-1} and R is the radius in pc (Larson 1981; Solomon et al. 1987; Myers & Goodman 1988; Fuller & Myers 1992). This empirical law is valid over a wide range of scales, although the nature of the nonthermal turbulence has not yet been well understood. For I04365 and I04368, the observed rotation on small scales is in the opposite sense to that of the surrounding lower density material (for I04368, see Ohashi et al. 1997; for I04365, see § 3.2.2). This implies that the large-scale rotation is not directly related to the dynamically infalling regions located deep inside the cores, and may have the characteristics of turbulence. Because the nonthermal motion decreases with size, dynamical collapse may take place inside a radius in which the effects of nonthermal pressure, including magnetic pressure, are negligible compared to those of thermal pressure, i.e., in which the velocity dispersion due to turbulence is comparable to or smaller than the sound speed.

With the observed relation $\Delta V = 1.2R^{0.4-0.5}$ and $R = 0.03$ pc, we obtain $\Delta V = 0.2$–0.3 km s^{-1}, smaller than 0.47 km s^{-1}, the line width for H_2 molecules at $T = 10$ K, estimated from its isothermal sound speed of 0.2 km s^{-1} at 10 K. According to the line width–size relation for nonthermal motions derived by Fuller & Myers (1992), $\Delta V_{NT} = 1.6R^{0.7}$, the line width by non-thermal motions at $R = 0.03$ pc is ~ 0.1 km s^{-1}, significantly smaller than the line width for H_2 molecules at 10 K. Thus the region inside the radius of ~ 0.03 pc has negligible turbulent support and could undergo dynamical collapse, leaving the outer part still supported by the turbulence.

Interestingly, the size scale for dynamical collapse, 0.03 pc, is similar to the typical clustering scale for young stars in the Taurus molecular cloud, 0.04 pc (Larson 1995). Despite this, dynamical collapse cannot be easily compatible with multiple star formation, especially when binary separation is comparable to the size scale of collapse. Recent three-dimensional calculation of the isothermal collapse of oblate

[12] We note that at present the number of samples is too small to extract a general conclusion. However, we observed the rotation of five protostellar envelopes, and the number of samples is a significant fraction of the total number (~ 15) of embedded protostellar sources associated with the Taurus molecular cloud.

cloud cores suggests that dynamically collapsing regions can fragment. In this calculation, however, fragmentation will occur at the inner part of a collapsing cloud, so that multiple stars with a small separation will form (Boss 1996). According to Larson (1995), the probability of finding a binary companion is the same for each logarithmic annulus around a young star when the annular radius is less than 0.04 pc. If the probability holds for the intrinsic separations of binaries, we would have difficulties in explaining it by way of the dynamical collapse scale of ~ 0.03 pc.

5. CONCLUSIONS

We have investigated the kinematics of circumstellar material around IRAS 04169+2702 and IRS 04365+2535 using millimeter interferometers. The main results are summarized as follows:

1. A $C^{18}O$ $J = 1$–0 elongated structure perpendicular to the axis of an associated outflow was detected around IRAS 04169+2702. It has a size and total mass of 2200 AU $\times$ 1100 AU and 0.024 $M_\odot$, respectively, and shows a velocity gradient along its major axis, suggesting that it is most probably a rotating disk or a flattened envelope. The rotation velocity is ~ 0.23 km s^{-1} at 370 AU with a correction for disk inclination, leading to a dynamical mass of ~ 0.02 $M_\odot$, a value that is incompatible with the expected mass of the central star, making it difficult to argue that the flattened structure is supported by rotation. We speculate that there is a strong infall component, although we observed no evidence for additional radial motion across the minor axis of the flattened envelope.

2. A compact ^{13}CO $J = 1$–0 condensation was detected around IRAS 04365+2535 with a size of 1400 AU together with fainter extended components probably associated with the molecular outflow. A lower limit to the gas mass of the condensation was 8.3×10^{-3} $M_\odot$. The condensation has an apparent velocity gradient in the direction perpendicular to the associated outflow axis, suggesting that it is probably a rotating disk or envelope. The rotation velocity is ~ 0.87 km s^{-1} at 580 AU with the assumed disk inclination angle of 50°, giving a dynamical mass of ~ 0.5 $M_\odot$, which is consistent with the total mass known to be contained within 580 AU. The ^{13}CO condensation can be explained, therefore, in terms of a rotationally supported disk.

3. The local specific angular momenta of the two observed sources together with other infalling envelopes and rotationally supported disks around five sources were compared with those of NH_3 dense cores with and without central sources. In contrast to the dense cores, whose local specific angular momenta have a power-law dependence on radius over the range 0.03 pc (6000 AU) to 0.4 pc (80,000 AU), the seven sources with infalling envelopes or rotationally supported disks have a relatively constant local specific angular momentum of $\sim 10^{-3}$ km s^{-1} pc over the radius range from 0.001 pc (200 AU) to 0.01 pc (2000 AU). Their local specific angular momenta are much smaller than those for dense cores but much larger than those obtained by extrapolating to the same radii from the power-law relation for larger scales. Thus the power-law relation cannot be extrapolated to the seven sources, and it seems to break at ~ 0.03 pc (6000 AU).

4. The curve of the local specific angular momenta suggests that a star-forming core can be divided into two zones at the radius of ~ 0.03 pc: a region inside this radius, where gas has relatively constant specific angular momentum, and an outer region, where the power-law relation applies. In the sense that local specific angular momentum is conserved within ~ 0.03 pc, this size scale can be regarded as characteristic for dynamical collapse in the Taurus molecular cloud. This size scale suggests that only the inner 0.03 pc region of a dense core undergoes dynamical collapse, while the outer region remains gravitationally stable. It is important to note that this size scale seems to be essentially the same from one source to another. It is also important that the radius of 0.03 pc encircles a typical stellar mass in Taurus if a dense core is supported by thermal pressure.

We acknowledge the staff members of Nobeyama Radio Observatory and Owens Valley Radio Observatory. Min S. Yun kindly supported our observations at OVRO. We also thank Ken-ichi Tatematsu, Takenori Nakano, and Shu-ichiro Inutsuka for fruitful discussions. An anonymous referee provided invaluable suggestions that improved the paper. N. O. is supported by a Smithsonian postdoctoral fellowship. Owens Valley Radio Observatory is supported by the National Science Foundation through grant AST 93-4109.

APPENDIX A

THE ^{13}CO $J = 1$–0 EMISSION FROM IRAS 04169+2702

Figure 7 shows the total intensity map of ^{13}CO integrated over the velocity range $V_{LSR} = 4.8$–8.9 km s^{-1}, superimposed on the ^{12}CO outflow map (Tamura et al. 1997). The ^{13}CO emission shows a relatively compact condensation at higher level contours, with its peak close to the central star, and a weaker diffuse component extending to the north and south. The compact condensation is elongated east-west (P.A. = 76°), in almost the same direction as the bipolar outflow axis. The eastern boundary of the diffuse component delineates very well the sharp western edge of the redshifted outflow.

At blueshifted velocities with respect to the systemic velocity of ~ 6.8 km s^{-1} measured at $\sim 17''$ resolution in $C^{18}O$ $J = 1$–0 with the Nobeyama 45 m telescope (N. Ohashi 1994, unpublished data), the channel maps of ^{13}CO presented in Figure 8 display weak emission at the central star position with additional weak features located to the north and south of the central star. A paucity of emission at the star at $V_{LSR} = 6.7$ km s^{-1} may be due to the resolving out of extended components with the interferometer because of the absence of short spacing data. In contrast, the redshifted emission shows rather complicated features, changing from an east-west elongated region at 7 km s^{-1} to a predominantly north-south ridge from 7.4 to 8.4 km s^{-1}, and finally weakening to a northwest small area at 8.7 km s^{-1}.

From Figures 7 and 8 we conclude that the ^{13}CO images include a blend of the emission from the surrounding envelope and outflow. For example, the central condensation elongated along the outflow axis in Figure 7 may suggest that it is part of the outflow, while the diffuse component, which is basically anticorrelated with the redshifted outflow, may be part of the

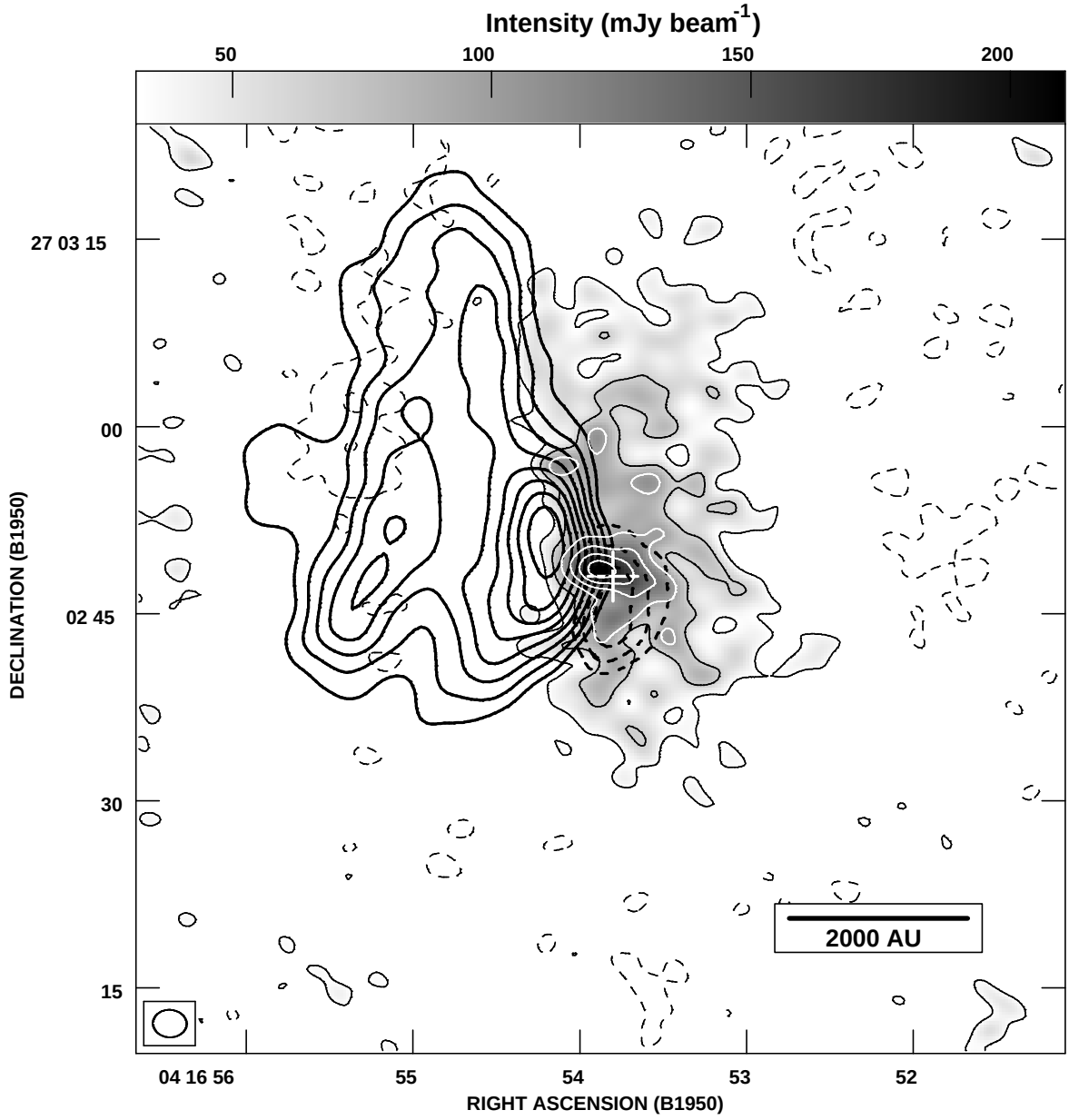

FIG. 7.—Total intensity ^{13}CO $J = 1$–0 of IRAS 04169+2702 in gray scale. For comparison, the ^{12}CO $J = 1$–0 blueshifted (*thick dashed contours*) and redshifted (*thick contours*) outflow maps (Tamura et al. 1997) are superimposed. The contours of the ^{13}CO intensity map are drawn at 2 σ steps from the 2 σ level (*solid contours*) and at -2 σ steps from the -2 σ level (*dashed contours*). The 1 σ level corresponds to 16 mJy beam^{-1}. The cross marks the position of the central star determined from the present 2.7 mm continuum observations.

molecular envelope evacuated in the outflow direction and may also contain gas interacting with the outflow. Further, the blueshifted velocity channel maps are elongated in the east-west direction, similar to the central condensation in the integrated intensity map, suggesting that these elongated blueshifted components are part of the outflow. The northeast peaks at 7.4 and 7.7 km s^{-1} in the redshifted channel maps are also likely to be part of the outflow, although it is difficult to make this case for the southwest peaks. Because of their likely contamination by the outflow emission, the ^{13}CO images cannot be used to investigate the kinematics of the circumstellar envelope around I04169. We have, as a result, used only the C^{18}O data to discuss the kinematics of the envelope in this paper.

APPENDIX B

ESTIMATION OF THE PROTOSTELLAR CORE MASS OF IRAS 04169+2702

The mass of the protostellar core of IRAS 04169+2702 was estimated assuming steady mass accretion as described by Stahler, Shu, & Taam (1980). The total accretion luminosity is given by $L = GM_* \dot{M}/R_*$, where G, M_*, $\dot{M}$, R_* are the

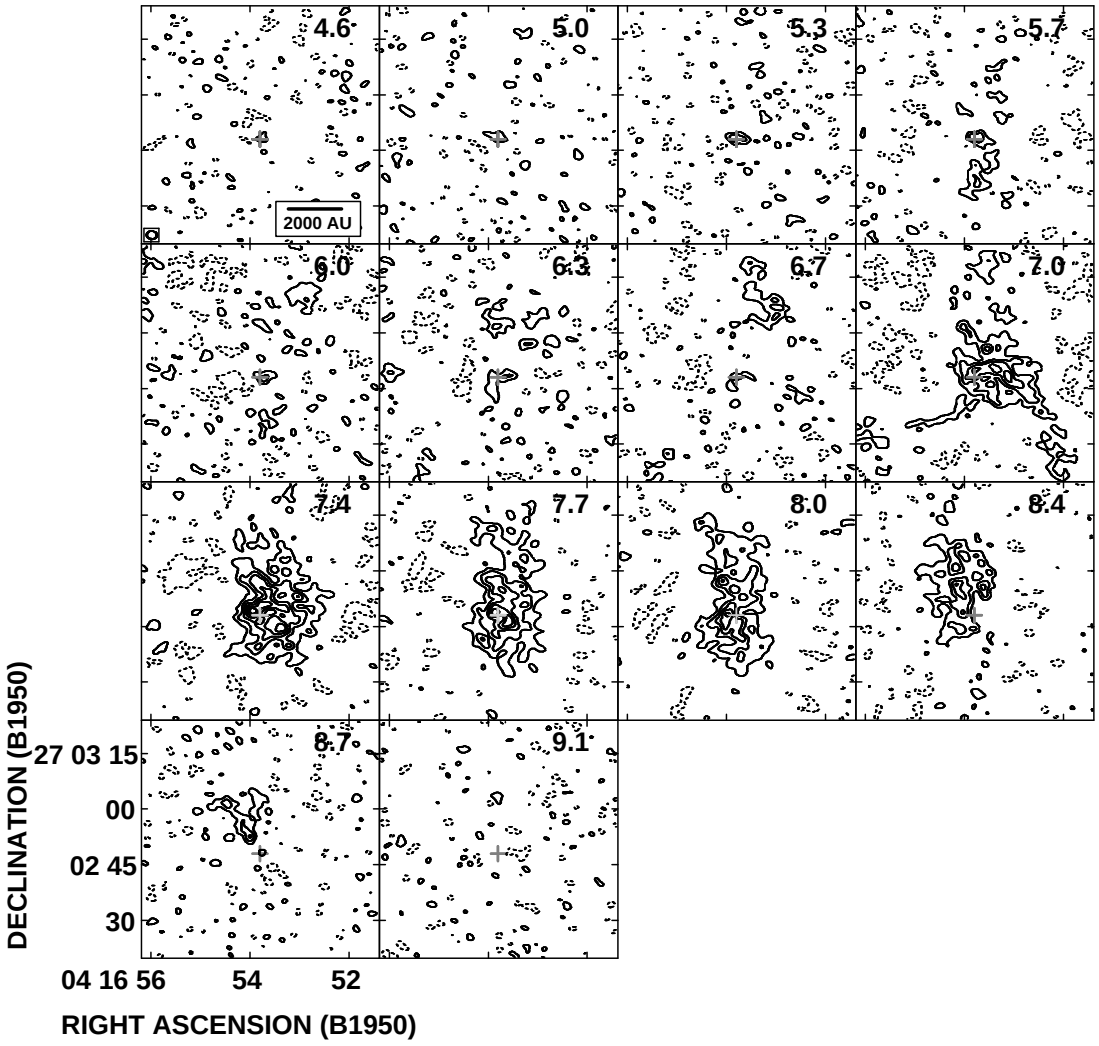

FIG. 8.—^{13}CO channel maps of IRAS 04169+2702 with a velocity resolution of $\sim$0.34 km s^{-1}. The central LSR velocity of each velocity channel is denoted at the top right corner in each corresponding panel. The systemic velocity is $\sim$6.8 km s^{-1}. Contours are at 2 σ steps from the 2 σ level (*solid contours*) and at -2 σ steps from the -2 σ level (*dashed contours*). The 1 σ level corresponds to $\sim$40 mJy beam^{-1} or 0.7 K in brightness. The cross in each panel indicates the position of the central star.

gravitational constant, stellar mass, mass accretion rate, and stellar radius, respectively. For steady mass accretion, the mass accretion rate $\dot{M}$ can be expressed as M_*/t, where t is the age of the protostar, i.e., the elapsed time from the onset of mass accretion onto the stellar core. We then derive the stellar mass from $M_* = (LR_* t/G)^{1/2}$, leading to a value of $\sim 0.1\ M_\odot$; the observed bolometric luminosity is 0.76 $L_\odot$ (Kenyon et al. 1993), and the assumed age and stellar radius are 10^5 yr and 4 $R_\odot$, respectively. For $R_* = 1\ R_\odot$ and $t = 10^4$ yr, we obtain the stellar mass of 0.015 $M_\odot$, which is still comparable to the required dynamical mass contained within the radius of 370 AU.

REFERENCES

Adams, F. C., Lada, C. J., & Shu, F. H. 1987, ApJ, 312, 788
Beckwith, S. V. W., Sargent, A. I., Chini, R. S., & Güsten, R. 1990, AJ, 99, 924
Benson, P. J., & Myers, P. C. 1989, ApJS, 71, 89
Bonner, W. B. 1956, MNRAS, 116, 351
Bontemps, S., André, P., Terebey, S., & Cabrit, S. 1996, A&A, 311, 858
Boss, A. P. 1996, ApJ, 468, 231
Chandler, C. J., Terebey, S., Barsony, M., Moore, T. J. T., & Gautier, T. N. 1996, ApJ, 471
Dutrey, A., Guilloteau, S., & Simon, M. 1994, A&A, 286, 149
Elias, J. H. 1978, ApJ, 224, 857
Fuller, G. A., & Myers, P. C. 1992, ApJ, 384, 523
Goldsmith, P. F., & Arquilla, R. 1985, in Protostar and Planets II, ed. D. C. Black & M. S. Matthews (Tucson: Univ. Arizona Press), 137
Goodman, A. A., Benson, P. J., Fuller, G. A., & Myers, P. C. 1993, ApJ, 406, 528
Hayashi, M. Ohashi, N., & Miyama, S. M. 1993, ApJ, 418, L71
Kawabe, R., Ishiguro, M., Omodaka, T., Kitamura, Y., & Miyama, S. M. 1993, ApJ, 404, L63
Keene, J., Hildebrand, R. H., & Whitcomb, S. E. 1982, ApJ, 252, L11
Kitamura, Y., Kawabe, R., & Saito, M. 1996, ApJ, 465, L137
Kenyon, S. J., Hartmann, L. W., Strom, K. M., & Strom, S. E. 1990, AJ, 99, 869
Kenyon, S. J., Calvet, N., & Hartmann, L. 1993, ApJ, 414, 676
Larson, R. B. 1981, MNRAS, 194, 809
———. 1985, MNRAS, 214, 379
———. 1995, MNRAS, 272, 213
Lay, O. P. Carlstrom, J. E., Hills, R. E., & Phillips, T. G. 1994, ApJ, 434, L75
Lin, D. N. C., Hayashi, M., Bell, K. R., & Ohashi, N. 1994, ApJ, 435, 821
Looney, L., Mundy, L. G., & Welch, W. J. 1997, ApJ, in press
Moriarty-Schieven, G. H., Wannier, P. G., Tamura, M., & Keene, J. 1992, ApJ, 400, 260
Moriarty-Schieven, G. H., Wannier, P. G., Keene, J., & Tamura, M. 1994, ApJ, 436, 800
Mundy, L. G., et al. 1996, ApJ, 464, L169
Myers, P. C., Fuller, G. A., Mathieu, R. D., Beichman, C. A., Benson, P. J., Schild, R. E., & Emerson, J. P. 1987, ApJ, 319, 340

Myers, P. C., & Goodman, A. A. 1988, ApJ, 329, 392
Myers, P. C., Linke, R. A., & Benson, P. J. 1983, ApJ, 264, 517
Ohashi, N., Hayashi, M., Ho, P. T. P., & Momose, M. 1997, ApJ, 475, 211
Ohashi, N., Hayashi, M., Ho, P. T. P., Momose, M., & Hirano, N. 1996a, ApJ, 466, 957
Ohashi, N., Hayashi, M., Kawabe, R., & Ishiguro, M. 1996b, ApJ, 466, 317
Ohashi, N., Kawabe, R., Hayashi, M., & Ishiguro, M. 1991, AJ, 102, 2054
Saito, M., Kawabe, R., Kitamura, Y., & Sunada, K. 1996, ApJ, 473, 464
Saito, M., Kawabe, R., Ishiguro, M., Miyama, S. M., Hayashi, M., Handa, T., Kitamura, Y., & Omadaka, T. 1995, ApJ, 453, 384
Solomon, P. M., Rivolo, A. R., Barrett, J., & Yahil, A. 1987, ApJ, 319, 730
Shu, F. H. 1977, ApJ, 214, 488
Stahler, S. W., Shu, F. H., & Taam, R. E. 1980, ApJ, 241, 637
Tamura, M., Ohashi, N., Hirano, N., Itho, Y., & Moriarity-Schieven, G. H. 1996, AJ, 112, 2076
Tamura, M., Ohashi, N., Hirano, N., Itho, Y., Moriarty-Schieven, G. H., & Momose, M. 1997, in preparation
Terebey, S., Chandler, C. J., & André, P. 1993, ApJ, 414, 759
Wilner, D. J., Ho, P. T. P., & Rodríguez, L. F. 1996, ApJ, 470, L117

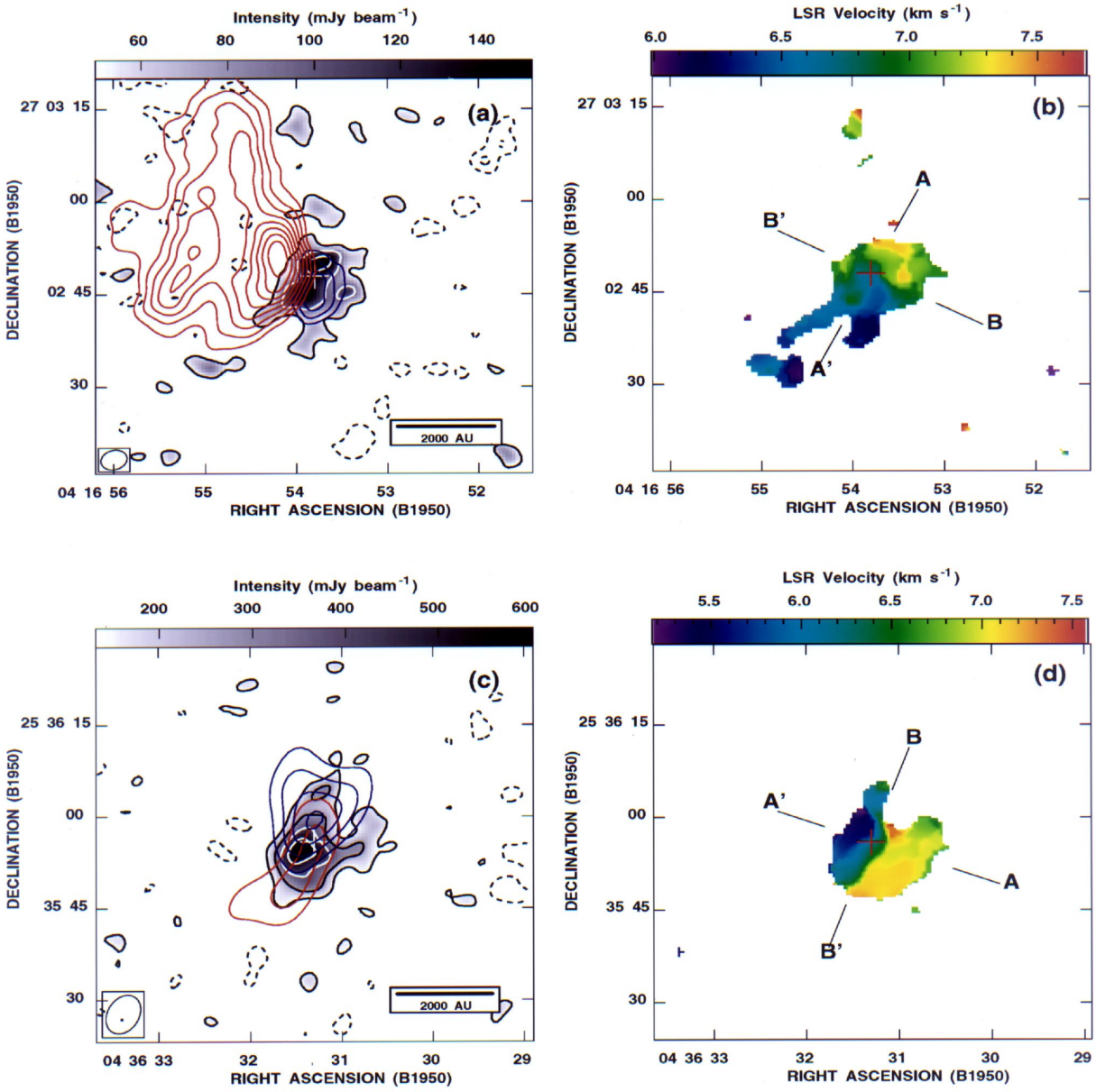

FIG. 1.—Total intensity and mean velocity maps of IRAS 04169+2702 and IRAS 04365+2535. The cross in each panel indicates the position of the central star estimated from the present 2.7 mm continuum observations. (*a*) $C^{18}O$ $J = 1$–0 integrated intensity map of IRAS 04169+2702 with gray scales, superimposed on the ^{12}CO outflow map (Tamura et al. 1997); the blue lobe is presented in blue contours and the red lobe in red contours. Contours of the $C^{18}O$ intensity map are drawn in 2 σ steps from the 2 σ level (*solid contours*) and at -2 σ steps from the -2 σ level (*dashed contours*). The 1 σ level corresponds to 25 mJy beam^{-1}. (*b*) Mean velocity map of $C^{18}O$ from IRAS 04169+2702 in pseudocolor. The systemic velocity of IRAS 04169+2702 is $\sim$6.8 km s^{-1}. (*c*) ^{13}CO $J = 1$–0 integrated intensity map of IRAS 04365+2535 with gray scales, superimposed on the ^{12}CO outflow map (Tamura et al. 1996). The blue and red lobes are contoured in blue and red, respectively. Contours of the ^{13}CO map are drawn in the same manner as in (*a*). The 1 σ level corresponds to 67 mJy beam^{-1}. (*d*) Mean velocity map of ^{13}CO from IRAS 04365+2535 is in pseudocolor. The systemic velocity of IRAS 04365+2535 is $\sim$6.4 km s^{-1}.

OHASHI et al. (see 462, 319)